Article

A soil-inspired dynamically responsive chemical system for microbial modulation

Yiliang Lin [1,11] ✉, Xiang Gao [1,11], Jiping Yue[2,11], Yin Fang[1,11], Jiuyun Shi[2], Lingyuan Meng [3], Clementene Clayton[2], Xin-Xing Zhang[1,2,4], Fengyuan Shi [5], Junjing Deng [6], Si Chen[6], Yi Jiang [6], Fabricio Marin[6], Jingtian Hu[7], Hsiu-Ming Tsai[8], Qing Tu [9], Eric W. Roth[10], Reiner Bleher [9,10], Xinqi Chen[10], Philip Griffin[3], Zhonghou Cai[6], Aleksander Prominski[1,2,4], Teri W. Odom [7,9] and Bozhi Tian [1,2,4] ✉

Interactions between the microbiota and their colonized environments mediate critical pathways from biogeochemical cycles to homeostasis in human health. Here we report a soil-inspired chemical system that consists of nanostructured minerals, starch granules and liquid metals. Fabricated via a bottom-up synthesis, the soil-inspired chemical system can enable chemical redistribution and modulation of microbial communities. We characterize the composite, confirming its structural similarity to the soil, with three-dimensional X-ray fluorescence and ptychographic tomography and electron microscopy imaging. We also demonstrate that post-synthetic modifications formed by laser irradiation led to chemical heterogeneities from the atomic to the macroscopic level. The soil-inspired material possesses chemical, optical and mechanical responsiveness to yield write–erase functions in electrical performance. The composite can also enhance microbial culture/biofilm growth and biofuel production in vitro. Finally, we show that the soil-inspired system enriches gut bacteria diversity, rectifies tetracycline-induced gut microbiome dysbiosis and ameliorates dextran sulfate sodium-induced rodent colitis symptoms within in vivo rodent models.

Interactions between the microbiota and their colonized environments mediate critical pathways in biogeochemical cycles, ecological resilience and human health[1,2]. Novel materials that can controllably modulate such microbial activity may contribute to both fundamental and applied research, including drug delivery[3], artificial photosynthesis[4–8], biohybrid fuel cells[9,10], carbon dioxide fixation[11–13] and living materials[14–18]. The microbially colonized environment of soil is a perfect example of a microbe–material interaction in nature, and it represents a mechanically and chemically integrated system that can remodel its properties in response to the external environment[19]. Spatially complex and dynamic environs within the soil's porous structures support the high diversity and density of soil microbiota[19,20], which in turn mediate

[1]The James Franck Institute, University of Chicago, Chicago, IL, USA. [2]Department of Chemistry, University of Chicago, Chicago, IL, USA. [3]Pritzker School of Molecular Engineering, University of Chicago, Chicago, IL, USA. [4]The Institute for Biophysical Dynamics, University of Chicago, Chicago, IL, USA. [5]Electron Microscopy Core, Research Resources Center, University of Illinois Chicago, Chicago, IL, USA. [6]Advanced Photon Source, Argonne National Laboratory, Lemont, IL, USA. [7]Department of Chemistry, Northwestern University, Evanston, IL, USA. [8]Department of Radiology, University of Chicago, Chicago, IL, USA. [9]Department of Materials Science and Engineering, Northwestern University, Evanston, IL, USA. [10]NUANCE Center, Northwestern University, Evanston, IL, USA. [11]These authors contributed equally: Yiliang Lin, Xiang Gao, Jiping Yue, Yin Fang. ✉e-mail: yilianglin@uchicago.edu; btian@uchicago.edu
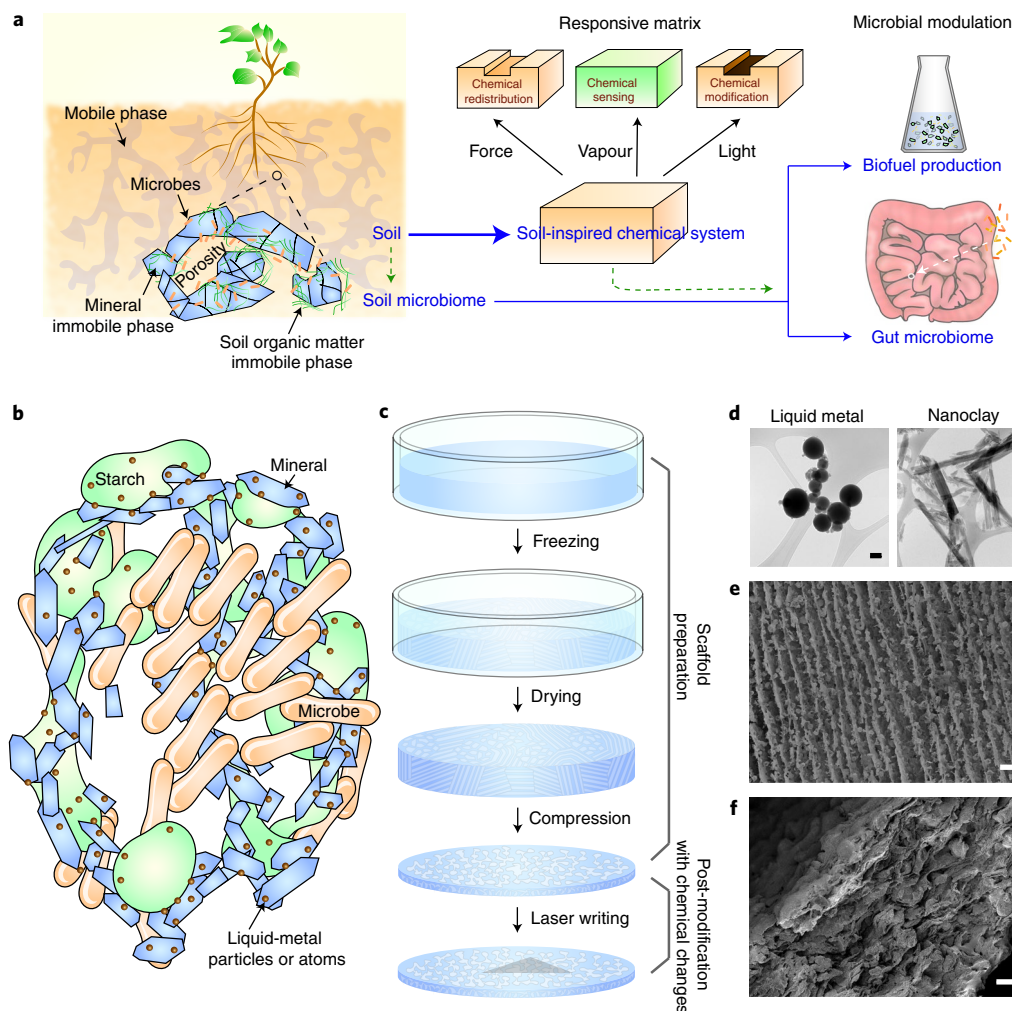
Fig. 1 | Soil-inspired dynamically responsive chemical system for microbial modulation. a, Schematic of the soil-inspired material. Nanoclay, starch and liquid metal loosely represent the inorganic, organic (that is, soil organic matter) and mobile phases, respectively, in soil. This soil-inspired material is responsive to force, vapour and light, which induce chemical redistribution within the complex. The soil-inspired material can be broadly applied for microbial modulation in, for example, biofuel production or homeostasis of the gut microbiome. **b**, Schematic showing the interaction between a microbial system and the soil-inspired material. **c**, Schematic of the fabrication process. Samples undergo freeze-drying and compression to create a structure similar to soil, followed by post-synthetic modification with laser writing to create chemical heterogeneity. **d**, TEM images showing the morphology of the liquid-metal particles and nanoclays before freeze-drying. Scale bars, 100 nm (left) and 200 nm (right). **e**, SEM image showing the formation of a layered structure after freeze-drying with ice templates. Scale bar, 50 μm. **f**, SEM image showing a more compact structure after compression. Scale bar, 20 μm.

essential biogeochemical cycling to provide nutrients such as nitrogen, phosphorous and sulfur to the soil system[21]. We hypothesize that a soil-inspired chemical system comprising porosity, chemically heterogeneous and dynamic properties, like those of natural soil, may serve as a responsive platform for the modulation of microbial systems[22,23].

In this Article we describe the design and synthesis of a soil-inspired material for microbial modulation using a bottom-up approach, and we demonstrate its capacity as a responsive microbial modulation platform in vitro and in vivo (Fig. 1a). We incorporate nanostructured minerals (a component of natural soil) as structural building blocks, alongside starch granules and liquid metals (Supplementary Table 1 and Fig. 1b), to endow the material with dynamic responsiveness. These three components loosely represent the inorganic, organic and mobile phases in natural soil. Using synchrotron-based correlative three-dimensional (3D) X-ray fluorescence and ptychographic tomography, as well as electron microscopy imaging, we confirm that the soil-inspired material is structurally similar to natural soil, with heterogeneous porosity. Like soil, the porous complex is an active matrix—it is responsive to force and vapour, which induce chemical

redistribution (Fig. 1a). The material possesses several unique properties due to the liquid-metal component, including mechanically enabled and chemically erasable electrical conductivity. The soil-inspired system can also be post-synthetically modified with laser irradiation to endow chemical heterogeneity from the atomic scale. In in vitro experiments, the soil-inspired material enhances biofilm growth, bacterial growth and biofuel production. In vivo, the material enriches gut bacterial diversity and rectifies bacterial dysbiosis under a pathophysiological condition. It also effectively protects the gastrointestinal epithelium and mitigates colitis symptoms in a dextran sulfate sodium (DSS)-induced rodent colitis model. The combined contributions from the material components (Supplementary Table 1) give rise to a new adaptive chemical system that can interface with microbiota for both biological and non-biological applications.

Results and discussion
Soil-inspired material synthesis and characterization
Our soil-inspired material comprises montmorillonite nanoclay, starch granules and liquid-metal (eutectic gallium–indium) particles.
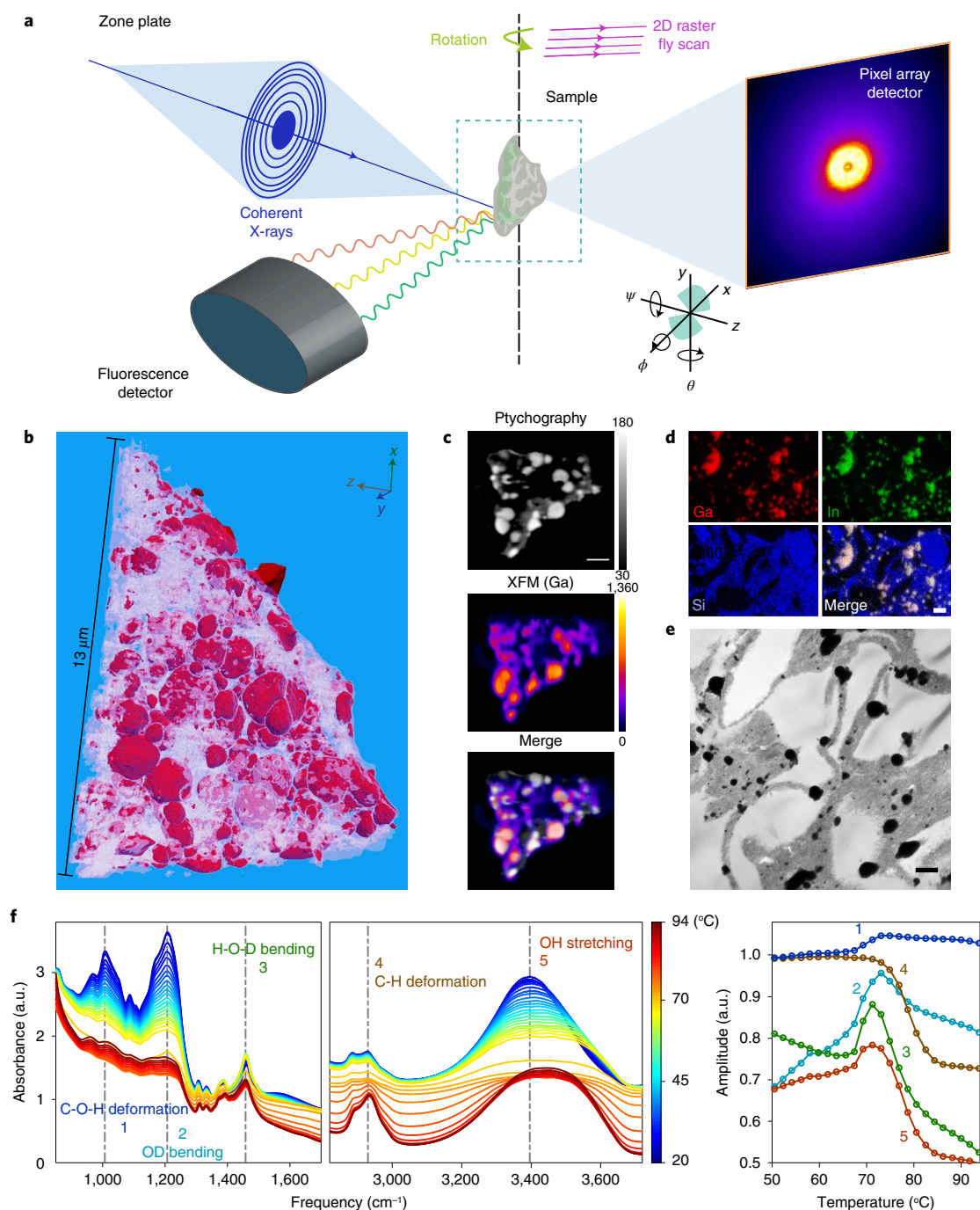
Fig. 2 | X-ray ptychographic, fluorescence tomography and in situ IR spectra reveal chemical composition and dynamics. a, Schematic of the simultaneous X-ray fluorescence and ptychography measurement experiment. A coherent monochromatic X-ray beam (10.7 keV) was focused by a Fresnel zone plate onto a spot of ~90 nm on a sample. The sample was raster fly-scanned in the x–y plane. Fluorescent signals and diffraction patterns were simultaneously recorded by a fluorescence detector and a pixel array detector, respectively. **b**, 3D ptychographic tomography demonstrates the distribution of liquid-metal particles in the soil-inspired material (liquid-metal particles are more electron-dense, shown as red). **c**, Sections of correlative 3D X-ray fluorescence and ptychographic tomography showing that the electron-dense particles in ptychography perfectly correlate with the gallium distribution in X-ray fluorescence imaging, confirming that the particles in the ptychography are gallium-based liquid-metal particles. Scale bar, 2 μm. **d**, Correlative fluorescence and ptychographic imaging of the microtomed samples showing the distribution of liquid metal (gallium and indium) and nanoclay (silicon). Scale bar, 2 μm. **e**, Cross-sectional TEM image of the soil-inspired material prepared by an ultramicrotome, showing well-distributed liquid metal (dark) inside the starch and nanoclay matrix (grey colour). Cross-sectional imaging further confirms the porosity of the soil-inspired material. Scale bar, 1 μm. **f**, In situ IR spectra confirm gelatinization of starch granules during the heating process. Evidence includes loss of starch granule crystallinity and formation of intermolecular hydrogen bonding between starch and heavy water.

Montmorillonite nanoclay can replicate the chemical composition of natural minerals and is a native composite of regular soil. The starch and liquid-metal components add responsiveness and additional functionality that natural soil does not possess. Specifically, starch granules undergo jamming in suspension[24,25] and gelatinization with increasing temperature[26]. Gallium-based liquid metals have a unique
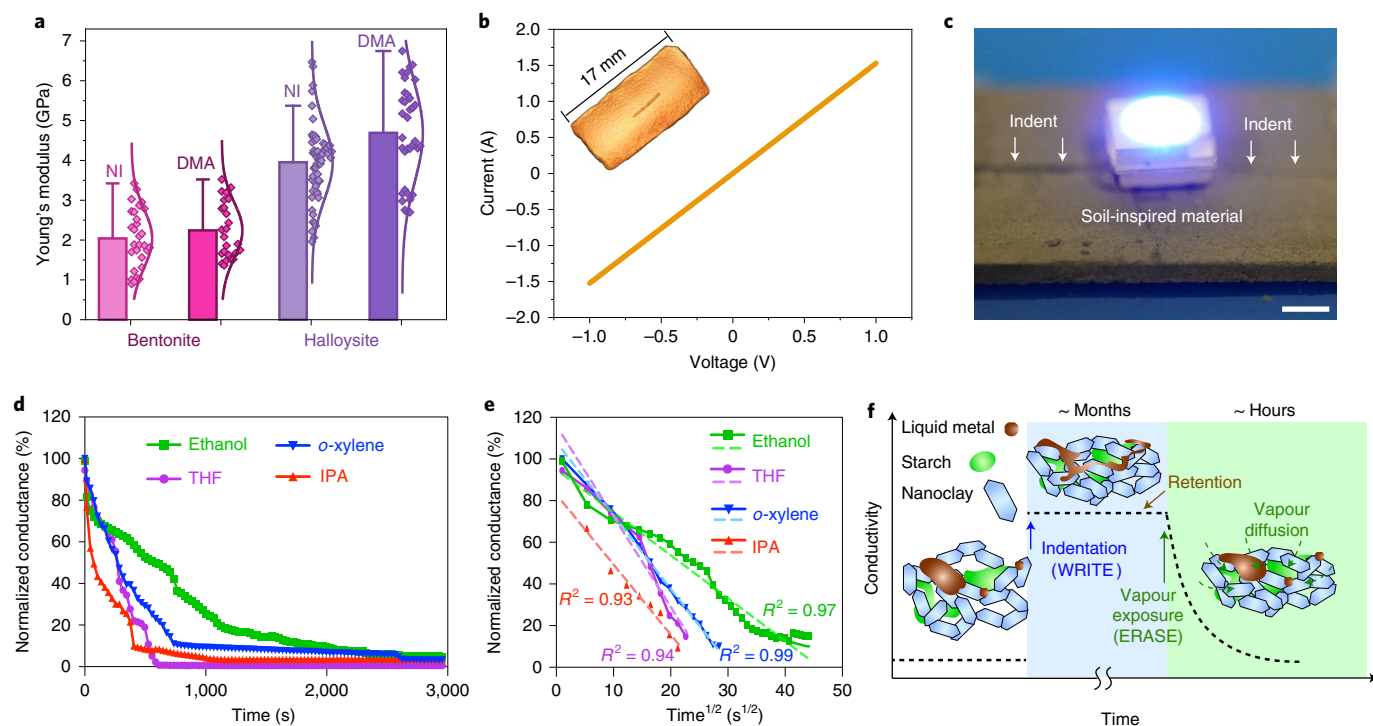
Fig. 3 | Soil-inspired material with tunable conductivity under mechanical and chemical stimuli. a, Statistical analysis showing that the Young's moduli of bentonite-containing and halloysite-containing soil-inspired material are ~2 GPa and ~5 GPa, respectively. NI, nanoindentation; DMA, dynamic mechanical analysis. n = 29, 25, 62 and 35, respectively, from left to right. Data are presented as mean values ± s.d. **b**, Mechanical sintering induces conductivity on the initially non-conductive soil-inspired material. The plot shows an I–V curve of the mechanically sintered pathway. Inset: X-ray microtomography image (microCT) of a soil-inspired material with a mechanically indented pathway. **c**, Optical images showing that the soil-inspired material can light up an LED with mechanically indented pathways. Scale bar, 1.5 mm. **d**, Solvent vapours, such as ethanol, o-xylene, THF and IPA, can erase the conductivity on the soil-inspired material. **e**, The change in conductance is linearly related to the square root of the time (from 0 s to the time when conductivity becomes almost zero) under solvent treatment, which well fits Fick's law of diffusion. This indicates that the erasing process may be dominated by a diffusion mechanism. **f**, Schematic showing that the soil-inspired material is a responsive matrix. Conductivity can be written with mechanical indentation and later erased chemically.

combination of metallic and fluidic properties and can undergo phase changes near or below room temperature, with unique properties[27–32]. As such, gallium has attracted considerable attention in bio-related applications[33,34], including drug delivery, positron emission tomography imaging and lung infection therapy.

To introduce porosity and chemical heterogeneity, essential for responsive properties and microbial interfaces in soil, we employed an ice-templating step[35–38] followed by hot compression (Fig. 1c and Supplementary Fig. 1). We vigorously mixed an aqueous suspension of nanoclay, starch granules and liquid-metal particles in a container. Before freeze-drying, the liquid-metal and clay particle sizes were at the nanoscale (Fig. 1d), whereas the starch granules had a size of ~10.1 μm (Supplementary Fig. 2). After freeze-drying, the sample formed a mineral-based layered scaffold (Fig. 1e), with starch granules and liquid-metal particles attached mainly to the mineral membrane or layer surfaces (Supplementary Fig. 3). We hypothesize that the ice-formation process may have selectively attracted the starch granules and liquid-metal particles to the ice surfaces (or the mineral/ice interface), resulting in a heterogeneous distribution of the components; this heterogeneous distribution is critical for the mechanical, chemical and optical responsive properties of the material, as discussed later (Supplementary Fig. 4b). Hot compression transformed the sample into a denser, multilayered, yet still porous scaffold (Fig. 1f). The starch granules deformed during the hot compression and toughened the composite due to glue-like binding between adjacent mineral layers. The large size of the starch granules also prevented a complete collapse of the composite into a non-porous composite. The as-made soil-inspired material can be processed into origami plates

with different geometries and assembled with polymer joints into corresponding 3D structures, such as a cube or a tetrahedron (Supplementary Fig. 5).

Synchrotron-based, correlative 3D X-ray fluorescence and ptychographic tomography (resolution of ~12.8 nm (ref. [39]), Fig. 2a) revealed dispersed liquid-metal particles with sizes ranging from tens of nanometres to several micrometres (Fig. 2b, red colour). Electron-dense particles observed by X-ray ptychography correlated with the gallium distribution seen in X-ray fluorescence imaging (Fig. 2c and Supplementary Figs. 6 and 7), and blank areas in the correlative sectioning images suggested porosity. The correlated images shown in the second (y–z) and third (x–y) rows of Supplementary Fig. 4 confirmed that the liquid-metal components mainly accumulate at the mineral layer surfaces. As discussed in the following, exposure of the liquid metals (that is, the responsive component) at the inner surfaces of the pores (Supplementary Fig. 4b) contributes to the observed responsive properties and microbial modulation activities of the soil-inspired material.

To further confirm the porosity of the soil-inspired material, we embedded it in an epoxy resin and prepared thin section slices (~200 nm) with an ultramicrotome. Fluorescence imaging (Fig. 2d), transmission electron microscopy (TEM) images (Fig. 2e) and focused-ion-beam (FIB) tomography (Supplementary Video 1) reaffirmed the porous nature of the material. The porosity of the material is ~54.6% according to 3D reconstruction with FIB tomography of a sample with volume of ~360 μm³ (Supplementary Fig. 8). X-ray ptychography and fluorescence imaging also verified that the electron-dense nanoparticles were gallium and indium, and the matrix hosting the liquid-metal nanoparticles was composed of nanoclay (Supplementary
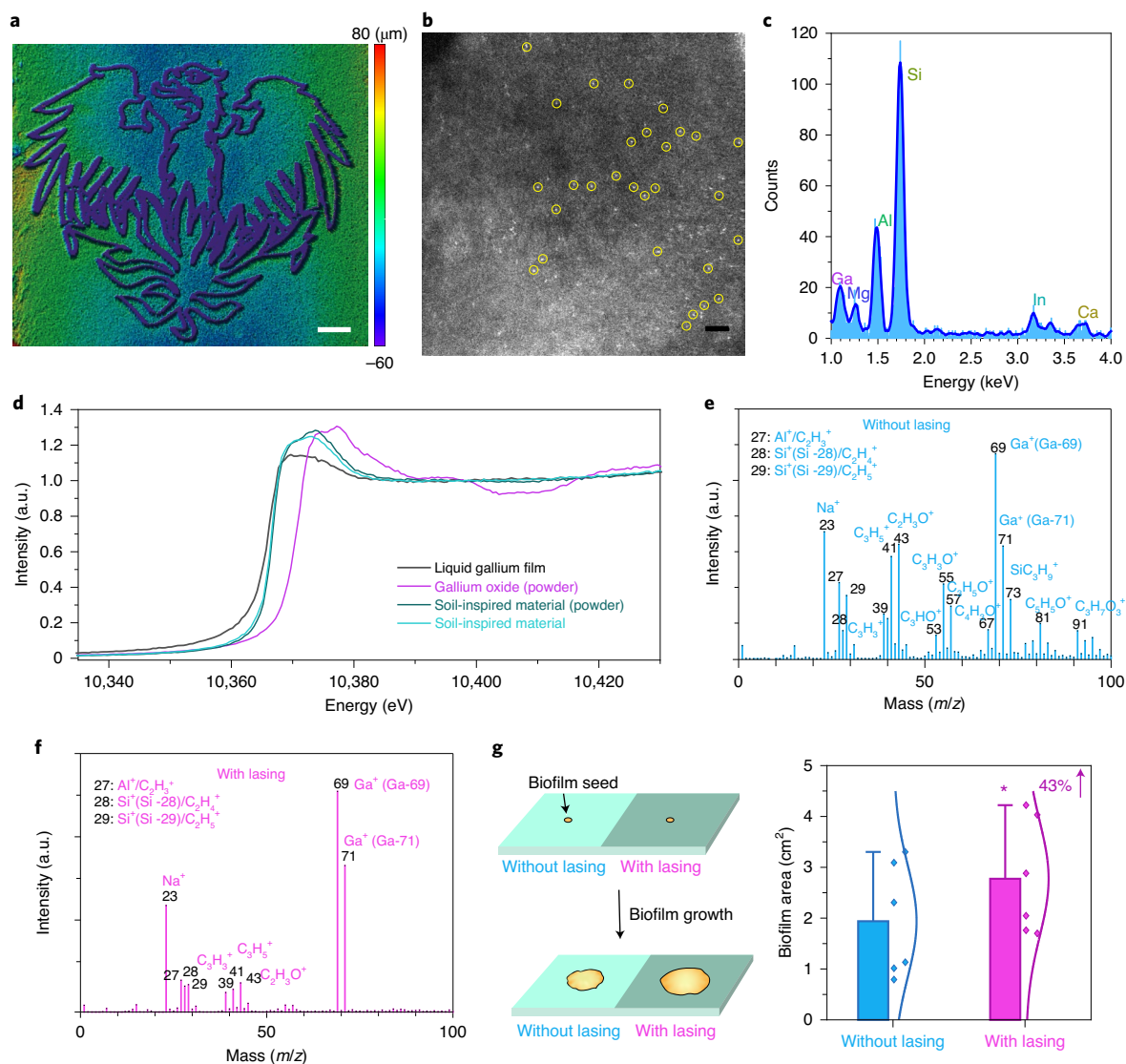
Fig. 4 | Laser-assisted chemical modification for biofilm growth enhancement. a, Laser microscopy images of soil-inspired material showing laser writing in spatially defined regions with The University of Chicago logo. Scale bar, 1 mm. **b**, High-resolution STEM image showing many single atoms with brighter contrast (circled with yellow). Scale bar, 2 nm. **c**, EDS in STEM confirms the existence of Ga and In single atoms and Al and Si elements in the supporting matrix, indicating stabilization of Ga and In atoms in nanoclay-containing matrices. **d**, XANES spectra show that the electronic structure of Ga in soil-inspired material containing Ga single atoms is different from the electronic structure of liquid gallium and gallium oxide. **e,f**, Positive spectra of TOF-SIMS from the soil-inspired material with and without laser writing demonstrate the chemical changes induced by post-modification with lasing. **g**, Biofilms on soil-inspired material with lasing are larger in area than those on the soil-inspired material without lasing (P = 0.031857). Paired t-test, two-tailed; n = 6. *, P < 0.05; ↑, the improvement of biofilm area by lasing. Data are presented as mean values ± s.d.

Figs. 9 and 10). When we prepared the composites by simple mixing of the components and hot compression, the material did not display the desired responsive properties (Supplementary Fig. 4c); the liquid-metal particles were encapsulated by minerals and starch granules, and thus lost their mobility and accessibility, whereas limited porosity resulted in the loss of responsiveness to external stimuli or perturbation.

As starch undergoes gelatinization with increasing temperature, we asked whether the hot compression step, in addition to condensing the framework, may have induced a fundamental change in the starch granule structure. We performed in situ infrared (IR) spectroscopy on hydrated starch granules with a heating/cooling cycle, employing heavy water to reveal the hydrogen-bond association during the crystalline-to-amorphous phase transition. During heating from 20 to 94 °C, we observed a loss of crystallinity in the starch granules, with the disappearance of spectral features at 1,007 cm^{-1}

(C–O–H deformation, peak 1, Fig. 2f) and 2,930 cm^{-1} (C–H deformation, peak 4)[40]. We also observed spectral changes associated with the OH stretching mode (~3,400 cm^{-1}, peak 5), OD bending mode (1,207 cm^{-1}, peak 2) and H–O–D bending mode (1,458 cm^{-1}, peak 3). These results suggest the formation of intermolecular hydrogen bonds between starch and heavy water (Fig. 2f, Supplementary Table 2 and Supplementary Fig. 11)[41]. We used singular value decomposition analysis to confirm that the starch granules underwent gelatinization during the fabrication process with a transition temperature of ~72 °C, in line with the phase change temperature of 70 °C established with differential scanning calorimetry (DSC; Supplementary Fig. 12). This gelatinization process was irreversible according to in situ cooling IR spectra (Supplementary Fig. 13). Gelatinization induced swelling of the granules, amylose crystallinity breaking and amylose diffusion out of the granules. As a result, the swollen granules, containing mostly amylopectin, collapsed but maintained their shape. Simultaneously, the diffused

amylose behaved as an organic glue that bound the granules to the nanoclay, contributing to the mechanical robustness of the soil-inspired material (Supplementary Fig. 14). The heat-induced transformation of starch positioned sticky and granular 'spacers' between adjacent mineral-based layers during the fabrication process, contributing to the porosity and liquid/bacterial transport capability (see the Bacterial modulation in laboratory culture section) of the soil-inspired material.

Mechanical, chemical and optical responsive properties

Naturally occurring soil is a mechanically and (bio)chemically integrated system with environmental responsiveness, and whose properties can be temporarily or permanently modified by nature. We further demonstrate that our soil-inspired material could act as a responsive matrix (similar to natural soil) and be post-modified for additional functionalities (Supplementary Table 1). The basic mechanical properties of the soil-inspired material can be tuned during synthesis. By selecting different nanoclays and altering the composition recipe (Supplementary Fig. 15), we can tune the Young's modulus of the material from ~2 GPa to ~5 GPa (Fig. 3a and Supplementary Fig. 16). Omission of the liquid-metal component resulted in a binary composite (that is, starch and minerals) with a smaller Young's modulus (1 GPa, approximately half that of the complete composite) that was less stable during compression tests (Supplementary Fig. 17). Considering the liquid metal itself has a Young's modulus of ~0 Pa (ref. [42]), this result suggests that the surface tension of the liquid metal may have 'tightened' the interaction between the starch and nanoclay to form a more robust matrix.

The mechanical force induced electrical conductivity, enabled by the liquid-metal component, in the initially non-conductive soil-inspired material (Fig. 3b and Supplementary Fig. 18). We demonstrate in Fig. 3c that the indented lines over the soil-inspired substrate can serve as interconnects to light up a light-emitting diode (LED). Without liquid metal, the material remains fully non-conductive. We speculate that local compression may spread the liquid-metal droplets through the pores, leading them to adhere to the mineral and starch surfaces; accordingly, mechanical force enables the chemical redistribution of liquid-metal droplets into a continuous pathway. Interestingly, this mechanically induced, electrically continuous pathway is sensitive to chemicals and can be erased by chemical vapours. We tested different solvents and found that solvents such as ethanol, isopropyl alcohol (IPA), o-xylene and tetrahydrofuran (THF) can erase the conductivity of the soil-inspired material (Fig. 3d). The linear relationship between conductance and the square root of time under vapour treatment suggested that the erasure of conductivity was dominated by diffusion (Fig. 3e). The solvent is known to influence the interfacial behaviour of gallium-based liquid metal[43]. We hypothesize that erasure of the conductivity may be related to the polarity and dielectric properties of the solvent and its wettability change on liquid metal interfaced with the nanoclay and starch matrix (Supplementary Fig. 19). Therefore, the soil-inspired material is a mechanically and chemically responsive matrix: we can write/encode conductivity via indentation (maintainable for months) and then erase the conductivity with chemical vapour exposure (Fig. 3f).

To recapitulate the substantial chemical and structural heterogeneities of soil, we used laser writing to post-synthetically modify the soil-inspired material in spatially defined regions. Laser writing provides a facile and efficient way to change local chemical and physical properties. We prepared a library of laser writing designs, including The University of Chicago logo (Fig. 4a and Supplementary Fig. 20). Aberration-corrected scanning transmission electron microscopy (aberration-corrected STEM) with high-angle annular dark-field (HAADF) imaging showed a dim nanoclay-containing matrix with a bright liquid-metal nanoparticle nearby (Fig. 4b and Supplementary Fig. 21). Zooming in on the matrix revealed well-dispersed single metal atoms (Fig. 4b, yellow circles). The average size of the single atoms is ~0.13 nm (Supplementary Fig. 22), and further analysis indicated that there are single atoms of two elements (Supplementary Fig. 23). Energy-dispersive X-ray spectroscopy (EDS) mapping of the single-atom-containing region confirmed the existence of both Ga and In elements as well as Si and Al, indicating that Ga and In single metal atoms were adsorbed and stabilized by the nanoclay-based matrix (a phyllosilicate containing silicon oxide and aluminium oxide) (Fig. 4c). These single atoms remained stable for months (Supplementary Fig. 24). X-ray absorption near-edge structure (XANES) spectra indicated partial oxidation of Ga compared to liquid-gallium film, which is in line with the unsaturated state of single metal atoms on a substrate (Fig. 4d). The synthesis of Ga and In single atoms from liquid metals has not been reported before, and our results lead us to believe that this single-atom-modified soil-inspired material may be used for heterogeneous catalysis, which is beyond the scope of the current study. Time-of-flight secondary ion mass spectrometry (TOF-SIMS) analysis revealed that laser writing notably removes carbohydrate species, especially those with high molecular weight, indicating that the starch granules are carbonized while the metal elements and nanoclay remain (Fig. 4e,f and Supplementary Fig. 25).

The laser writing also produced electrically conductive patterns on demand, which is probably due to the carbonization of the starch component and the nano-/atomic level redistribution of the liquid-metal component. The well-controlled conductive features over the soil-inspired material suggest its potential for patternable circuits (Supplementary Fig. 26a). Although laser writing produced

Fig. 5 | Soil-inspired material for gut microbiome modulation and DSS-induced colitis therapy in vivo. a, LEfSe taxa analysis confirms that the soil-inspired material enriches bacterial diversity under a pathological condition (tetracycline-induced gut microbiome dysbiosis) in vivo. **b–e**, Statistical analysis of *g_Oscillibacter* (**b**, $P = 0.0005$), *g_Allobaculum* (**c**, $P = 0.0421$), *g_Blautia* (**d**, $P = 0.0004$) and *g_Enterorhabdu* (**e**, $P = 0.0271$) modulation demonstrates that the soil-inspired material can rectify the dysbiosis of *g_Allobaculum* and *g_Oscillibacter*. Boxes bound the interquartile range (IQR) divided by the median, and whiskers extend to $1.5 \pm$ IQR. All data points are plotted ($n = 4$ for Tet_SIM and Tet_Vehicle group and $n = 3$ for healthy group). *, $P < 0.05$; **, $P < 0.01$; ***, $P < 0.001$. SIM, soil-inspired material. Two-tailed Student's *t*-test. **f**, The change in mouse body-weight percentage over seven consecutive days with oral administration of the soil-inspired material, the soil-inspired material without starch ('No starch'), without nanoclay ('No nanoclay') and without liquid metal ('No liquid metal') in DSS-induced ulcerative colitis. The results show that the soil-inspired material significantly mitigated mouse body-weight loss in DSS-induced colitis. Data are presented as mean $\pm$ s.e.m. ($n = 10$). P values are determined by ordinary one-way ANOVA with Tukey's multiple comparisons test; all the Tukey's multiple comparisons shown in the figure are between DSS control and corresponding experimental groups. NS, not significant or $P > 0.05$.

g, Soil-inspired material significantly mitigated the shortened colon length induced by ulcerative colitis. Specifically, the experimental group without starch (No starch) shows the shortest colon length, suggesting an essential role for starch in ulcerative colitis management. **h**, Mice with ulcerative colitis treated with soil-inspired material had significantly less faecal blood than other groups. Data are presented as mean $\pm$ s.e.m. ($n = 10$). P values are determined by ordinary one-way ANOVA with Tukey's multiple comparisons test; all the Tukey's multiple comparisons shown in the figure are between DSS control and corresponding experimental groups. NS, not significant or $P > 0.05$. **i**, Soil-inspired material mitigated diarrhoea in mice with ulcerative colitis. **j**, Histology of the colon shows that the soil-inspired material has a therapeutic effect, in terms of histological injuries, compared with the DSS control model. Scale bars, 100 μm. **k**, Histology injury score, showing that the soil-inspired material (that is, all components) achieved the best therapeutic effect on DSS-induced ulcer colitis. Boxes in **g**, **i** and **k** bound IQR divided by the median, and whiskers extend to $1.5 \pm$ IQR. All data points are plotted ($n = 5$). P values are determined by ordinary one-way ANOVA with Tukey's multiple comparisons test; all the Tukey's multiple comparisons shown in the figure are between DSS control and corresponding experimental groups. NS, not significant or $P > 0.05$.

stable properties and electrical devices in air, we can remove the laser-modified conductive patterns and recycle the soil-inspired substrates through sonication and high-speed vortex mixing in water (Supplementary Fig. 26b), suggesting potential applications in recyclable electronics utilizing optical patterning (Supplementary Fig. 26c).

Bacterial modulation in laboratory culture

We next investigated the ability of our soil-inspired chemical system to modulate microbial systems (Supplementary Table 1), given its advantages in porosity and responsiveness. We first cultured *Bacillus subtilis*—Gram-positive soil bacteria that attract distant motile cells
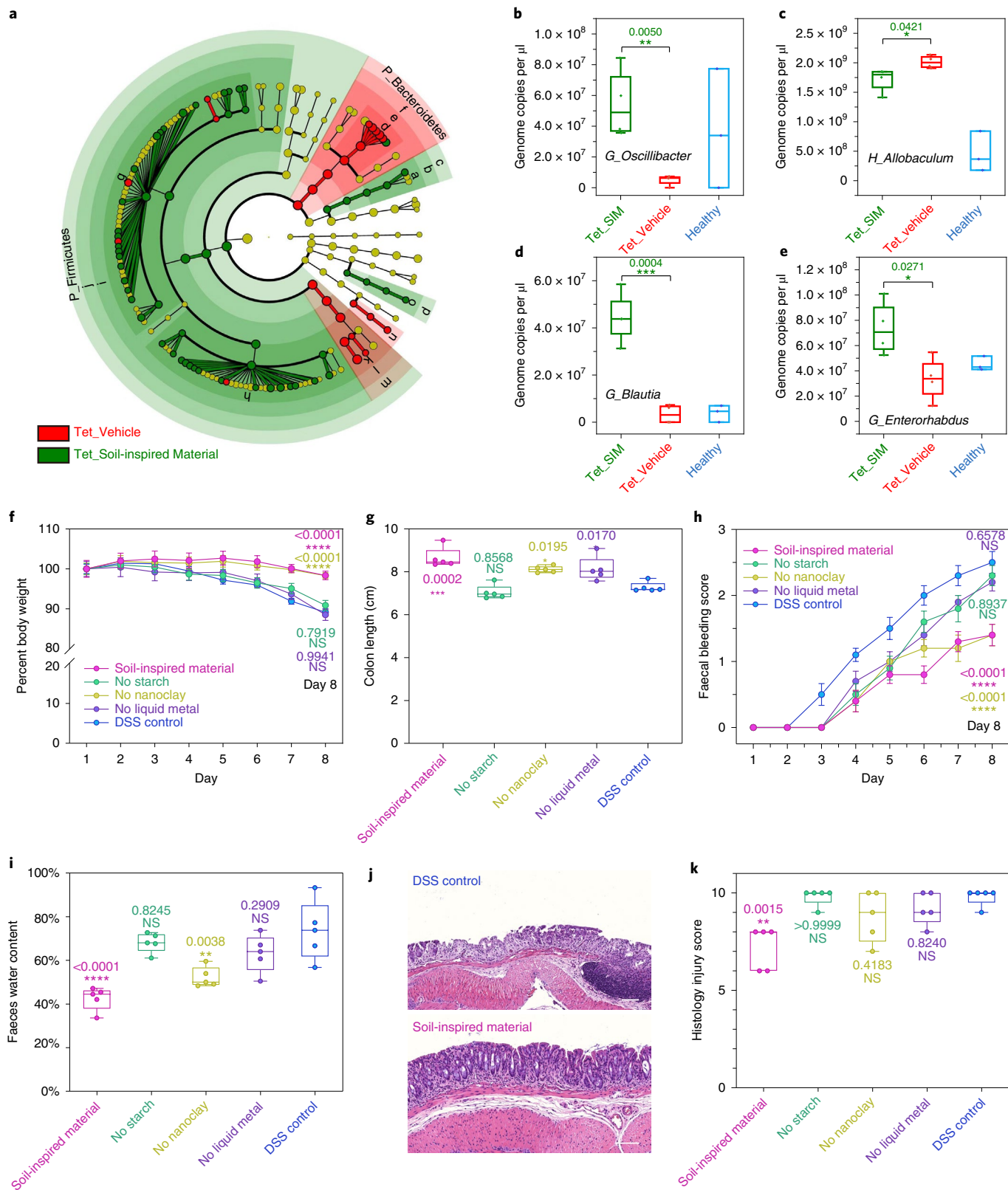
through electrical signalling in biofilms[44,45]—on soil-inspired material with and without laser treatment. As shown in Fig. 4g, biofilms grown on soil-inspired materials with lasing (5% power) had larger film areas than biofilms grown on soil-inspired materials without lasing (~43% increase). Meanwhile, laser power that was too high or too low (10% or 2% power) did not achieve the same level of enhancement (Supplementary Fig. 27). We also confirmed that the biofilm grown on soil-inspired material without laser and with different laser power levels shows no significant difference in cell number/density (Supplementary Fig. 28). Additional benchmark experiments (Supplementary Figs. 29 and 30) suggested that neither carbonization from starch granules, the presence of liquid-metal particles, nor increased conductivity alone could yield the observed bacterial growth enhancement. As such, it is possible that the single metal atoms produced by the lasing play an essential role in enhancing *B. subtilis* biofilm growth. We also studied the effect of the soil-inspired material in flask culture and found that the material enhanced *B. subtilis* growth better than carbon paper or hydrogel, although not as well as real soil (Supplementary Fig. 31). This microbial growth enhancement can be extended to Gram-negative *Escherichia coli* bacteria. The soil-inspired material promoted *E. coli* growth (Supplementary Fig. 32a) and increased biofuel synthesis (Supplementary Fig. 32b). These results indicate that the soil-inspired material may serve as a non-genetic tool to modulate microbial systems.

Bacterial modulation in vivo with gut microbiota

Bacillus subtilis is also a gut commensal bacterium. Based on the in vitro results (Fig. 4g and Supplementary Fig. 31), we hypothesized that the soil-inspired material could influence the in vivo biochemical environment and consequently the diversity and richness of the gut microbiome, which plays an essential role in priming the immune system, regulating gut endocrine function, modulating metabolism and eliminating toxins[46]. We first confirmed the in vivo biosafety and biocompatibility of the soil-inspired material in the C57B6/J mouse model. There was no statistical difference in body weight (Supplementary Fig. 33a), colon length (Supplementary Fig. 33b,c), colon histology (Supplementary Fig. 33d), distal/proximal crypt depth (Supplementary Fig. 34a), nuclei per crypt (Supplementary Fig. 34b) or histology of other internal organs (Supplementary Figs. 35 and 36) between soil-inspired material-treated mice and control mice. Ribosomal 16S sequencing of faecal samples showed no significant difference in either absolute gene abundance or alpha-diversity of the total faecal bacterium population (Supplementary Fig. 37). A taxonomy abundance heatmap showed no obvious changes in genera abundance among the richest genera, further indicating that the soil-inspired material did not result in noticeable gut microbiota dysbiosis (Supplementary Fig. 38).

After confirming the biosafety and biocompatibility of the soil-inspired material, we next tested the biochemical impact of the soil-inspired material in a pathologically relevant condition in mice, tetracycline-induced gut microbiome dysbiosis. Tetracycline causes significant microbiome dysbiosis; 16S sequencing data showed a significant reduction in absolute gut microbiota abundance (Supplementary Fig. 39) and abundance of the top richest genera (Supplementary Figs. 40 and 41). In mice suffering from tetracycline-induced dysbiosis, oral administration of the soil-inspired material significantly boosted gut microbial abundance compared with the vehicle control (Supplementary Fig. 42), based on microbial alpha-diversity quantification of faecal ribosomal 16S sequencing results. Linear discriminant analysis effect size (LEfSe) revealed a broader distribution of taxa, which indicated a significantly richer microbiota diversity in faeces from the soil-inspired material-treated mice (Fig. 5a). The enhancement of biodiversity might be attributed to the spatial partitioning offered by the porosity of soil-inspired materials[47]. High gut microbiota diversity, high gut microbiota gene richness and stable microbiome function are all indicators of healthy microbiota[46]. The ability of the soil-inspired material to enhance the diversity of gut microbiota under

a pathological condition demonstrates promise for material-enabled biochemical modulation of the gut microbiota. A taxonomy abundance heatmap comparing the relative abundances of the top richest genera between soil-inspired material-treated mice and control mice showed statistical differences in the abundance of *Oscillibacter*, *Allobaculum*, *Blautia* and *Enterorhabdus* (Supplementary Fig. 43). The soil-inspired material significantly rectified the tetracycline-induced dysbiosis of *Oscillibacter* and *Allobaculum* (Fig. 5b,c) and significantly enriched the abundance of *Enterorhabdus* and *Blautia* in the gut (Fig. 5d,e); the latter result requires further systematic investigation given the limited studies in the literature[48,49]. Our results demonstrate that the soil-inspired chemical system could modulate gut bacteria in a bifacial manner, rectifying the dysbiosis of *Allobaculum* and *Oscillibacter* while boosting levels of *Enterorhabdus* and *Blautia*.

To evaluate the potential of the soil-inspired material in more severe gastrointestinal conditions, we used the dextran sulfate sodium (DSS)-induced ulcerative colitis rodent model. We also included benchmark control groups to delineate the contributions from individual components. Specifically, mice, given 2% DSS drinking water ad libitum, were orally administrated with either (1) soil-inspired material (starch, nanoclay and liquid metal), (2) no starch (nanoclay and liquid metal), (3) no nanoclay (starch and liquid metal), (4) no liquid metal (starch and nanoclay) or (5) water (that is, DSS control group). In comparison to the DSS control group, mice treated with soil-inspired material presented significantly milder colitis symptoms, including less body-weight loss (Fig. 5f), longer colon length (Fig. 5g), lower faecal bleeding score (Fig. 5h) and lower faeces water content (Fig. 5i). These results indicate the therapeutic effects of soil-inspired materials in DSS-induced rodent colitis. Histology staining (Fig. 5j and Supplementary Fig. 44) and analysis (injury scoring in Fig. 5k, epithelial thickness in the proximal and distal colon in Supplementary Fig. 45) confirmed that the soil-inspired material improved the pathological appearance of the colon. The therapeutic efficacy of the complete soil-inspired material was greater than that of material that lacked components (Fig. 5f–i). We collected faeces from all groups for 16S sequencing to explore the effects of the different components on the gut microbiome. DSS and oral administration of soil-inspired material altered the gut microbiome composition (Supplementary Fig. 46), but they did not lead to a significant difference in the bacterial abundance or alpha-diversity (Supplementary Fig. 47). *g_Romboustsia* dysbiosis was exacerbated in the group treated with a material that did not contain liquid metal (Supplementary Fig. 48), which indicates that liquid metal may have a positive effect on *g_Romboustsia* dysbiosis. *g_Romboustsia* is a recently described bacterial genus[50], and its intestinal functions are not fully understood. One clinical study has reported that intestinal *Romboutsia* abundance is positively correlated with obesity and high serum lipids[51]. Another study reported increased *Romboutsia* abundance in DSS-induced mouse colitis[52], which is consistent with our result. The dysbiosis rectification with soil-inspired material containing liquid metal suggests its potential for intervention in inflammatory bowel disease through microbial modulation. Oral administration of soil-inspired material was visualized using time-lapse X-ray microtomography imaging. The soil-inspired material can arrive in the colon and accumulate in faeces within 6 hours (Supplementary Figs. 49 and 50). These test results indicate that the soil-inspired material and gut microbes are physically very close to the colon, which facilitates the material interacting and/or affecting the gut microbiome. Our results on the management of ulcerative colitis symptoms with soil-inspired materials suggest that this chemical system may find broad applications in intestinal pathophysiological conditions involving gut microbiota dysbiosis and inflammatory bowel conditions.

Outlook

This work presents the synthesis and characterization of a soil-inspired chemical system (Supplementary Table 1). We demonstrate its utility

as a dynamically responsive material platform for microbial modulation in vitro and in vivo. The soil-inspired chemical system shows promise as a therapy for gastrointestinal disease, suggesting a therapeutic alternative to existing techniques[53–57]. Beyond gut microbiota, this chemical system may be extended to the study of other microbiomes, such as skin and soil microbiota, which would have implications from human health to the stability and productivity of agro-ecosystems[58].

Online content

Any methods, additional references, Nature Research reporting summaries, source data, extended data, supplementary information, acknowledgements, peer review information; details of author contributions and competing interests; and statements of data and code availability are available at https://doi.org/10.1038/s41557-022-01064-2.

References

1. Rodriguez-Caballero, E. et al. Dryland photoautotrophic soil surface communities endangered by global change. *Nat. Geosci.* **11**, 185–189 (2018).
2. Zheng, D., Liwinski, T. & Elinav, E. Interaction between microbiota and immunity in health and disease. *Cell Res.* **30**, 492–506 (2020).
3. Jimenez, M., Langer, R. & Traverso, G. Microbial therapeutics: new opportunities for drug delivery. *J. Exp. Med.* **216**, 1005–1009 (2019).
4. Sakimoto, K. K., Wong, A. B. & Yang, P. Self-photosensitization of nonphotosynthetic bacteria for solar-to-chemical production. *Science* **351**, 74–77 (2016).
5. Zhang, H. et al. Bacteria photosensitized by intracellular gold nanoclusters for solar fuel production. *Nat. Nanotechnol.* **13**, 900–905 (2018).
6. Cestellos-Blanco, S., Zhang, H., Kim, J. M., Shen, Y. & Yang, P. Photosynthetic semiconductor biohybrids for solar-driven biocatalysis. *Nat. Catal.* **3**, 245–255 (2020).
7. Liu, C., Colón, B. C., Ziesack, M., Silver, P. A. & Nocera, D. G. Water splitting-biosynthetic system with CO_2 reduction efficiencies exceeding photosynthesis. *Science* **352**, 1210–1213 (2016).
8. Guo, J. et al. Light-driven fine chemical production in yeast biohybrids. *Science* **362**, 813–816 (2018).
9. Wang, T. et al. Bacteria-derived biological carbon building robust Li-S batteries. *Nano Lett.* **19**, 4384–4390 (2019).
10. Ding, M. et al. Nanoelectronic investigation reveals the electrochemical basis of electrical conductivity in *Shewanella* and *Geobacter*. *ACS Nano* **10**, 9919–9926 (2016).
11. Liu, C. et al. Nanowire–bacteria hybrids for unassisted solar carbon dioxide fixation to value-added chemicals. *Nano Lett.* **15**, 3634–3639 (2015).
12. Su, Y. et al. Close-packed nanowire-bacteria hybrids for efficient solar-driven CO_2 fixation. *Joule* **4**, 800–811 (2020).
13. Cestellos-Blanco, S., Zhang, H. & Yang, P. Solar-driven carbon dioxide fixation using photosynthetic semiconductor bio-hybrids. *Faraday Discuss.* **215**, 54–65 (2019).
14. Tang, T.-C. et al. Materials design by synthetic biology. *Nat. Rev. Mater.* **6**, 332–350 (2021).
15. Huang, J. et al. Programmable and printable *Bacillus subtilis* biofilms as engineered living materials. *Nat. Chem. Biol.* **15**, 34–41 (2019).
16. Liu, X. et al. Stretchable living materials and devices with hydrogel-elastomer hybrids hosting programmed cells. *Proc. Natl Acad. Sci. USA* **114**, 2200–2205 (2017).
17. Wang, Y. et al. Living materials fabricated via gradient mineralization of light-inducible biofilms. *Nat. Chem. Biol.* **17**, 351–359 (2021).
18. Gilbert, C. et al. Living materials with programmable functionalities grown from engineered microbial co-cultures. *Nat. Mater.* **20**, 691–700 (2021).
19. O'Donnell, A. G., Young, I. M., Rushton, S. P., Shirley, M. D. & Crawford, J. W. Visualization, modelling and prediction in soil microbiology. *Nat. Rev. Microbiol.* **5**, 689–699 (2007).
20. Young, I. M. & Crawford, J. W. Interactions and self-organization in the soil-microbe complex. *Science* **304**, 1634–1637 (2004).
21. Chaparro, J. M., Sheflin, A. M., Manter, D. K. & Vivanco, J. M. Manipulating the soil microbiome to increase soil health and plant fertility. *Biol. Fertil. Soils* **48**, 489–499 (2012).
22. Wargo, J. A. Modulating gut microbes. *Science* **369**, 1302–1303 (2020).
23. Gupta, A., Osadchiy, V. & Mayer, E. A. Brain–gut–microbiome interactions in obesity and food addiction. *Nat. Rev. Gastroenterol. Hepatol.* **17**, 655–672 (2020).
24. Peters, I. R., Majumdar, S. & Jaeger, H. M. Direct observation of dynamic shear jamming in dense suspensions. *Nature* **532**, 214–217 (2016).
25. James, N. M., Han, E., de la Cruz, R. A. L., Jureller, J. & Jaeger, H. M. Interparticle hydrogen bonding can elicit shear jamming in dense suspensions. *Nat. Mater.* **17**, 965–970 (2018).
26. Lelievre, J. Starch gelatinization. *J. Appl. Polym. Sci.* **18**, 293–296 (1974).
27. Daeneke, T. et al. Liquid metals: fundamentals and applications in chemistry. *Chem. Soc. Rev.* **47**, 4073–4111 (2018).
28. Zavabeti, A. et al. A liquid metal reaction environment for the room-temperature synthesis of atomically thin metal oxides. *Science* **358**, 332–335 (2017).
29. Markvicka, E. J., Bartlett, M. D., Huang, X. & Majidi, C. An autonomously electrically self-healing liquid metal–elastomer composite for robust soft-matter robotics and electronics. *Nat. Mater.* **17**, 618–624 (2018).
30. Dickey, M. D. Emerging applications of liquid metals featuring surface oxides. *ACS Appl. Mater. Interfaces* **6**, 18369–18379 (2014).
31. Chen, S., Wang, H.-Z., Zhao, R.-Q., Rao, W. & Liu, J. Liquid metal composites. *Matter* **2**, 1446–1480 (2020).
32. Hirsch, A., Dejace, L., Michaud, H. O. & Lacour, S. P. Harnessing the rheological properties of liquid metals to shape soft electronic conductors for wearable applications. *Acc. Chem. Res.* **52**, 534–544 (2019).
33. Yan, J., Lu, Y., Chen, G., Yang, M. & Gu, Z. Advances in liquid metals for biomedical applications. *Chem. Soc. Rev.* **47**, 2518–2533 (2018).
34. Goss, C. H. et al. Gallium disrupts bacterial iron metabolism and has therapeutic effects in mice and humans with lung infections. *Sci. Transl. Med.* **10**, eaat7520 (2018).
35. Wegst, U. G. K., Bai, H., Saiz, E., Tomsia, A. P. & Ritchie, R. O. Bioinspired structural materials. *Nat. Mater.* **14**, 23–36 (2015).
36. Munch, E. et al. Tough, bio-inspired hybrid materials. *Science* **322**, 1516–1520 (2008).
37. Bai, H., Chen, Y., Delattre, B., Tomsia, A. P. & Ritchie, R. O. Bioinspired large-scale aligned porous materials assembled with dual temperature gradients. *Sci. Adv.* **1**, e1500849 (2015).
38. Mao, L.-B. et al. Synthetic nacre by predesigned matrix-directed mineralization. *Science* **354**, 107–110 (2016).
39. Deng, J. et al. Correlative 3D X-ray fluorescence and ptychographic tomography of frozen-hydrated green algae. *Sci. Adv.* **4**, eaau4548 (2018).
40. van Soest, J. J. G., Tournois, H., de Wit, D. & Vliegenthart, J. F. G. Short-range structure in (partially) crystalline potato starch determined with attenuated total reflectance Fourier-transform IR spectroscopy. *Carbohydr. Res.* **279**, 201–214 (1995).

41. Ramakers, L. A. I. et al. 2D-IR spectroscopy shows that optimized DNA minor groove binding of Hoechst 33258 follows an induced fit model. *J. Phys. Chem. B* **121**, 1295–1303 (2017).

42. Wagner, S. & Bauer, S. Materials for stretchable electronics. *MRS Bull.* **37**, 207–213 (2012).

43. Khan, M. R., Trlica, C., So, J.-H., Valeri, M. & Dickey, M. D. Influence of water on the interfacial behavior of gallium liquid metal alloys. *ACS Appl. Mater. Interfaces* **6**, 22467–22473 (2014).

44. Humphries, J. et al. Species-independent attraction to biofilms through electrical signaling. *Cell* **168**, 200–209 (2017).

45. Nimje, V. R. et al. Stable and high energy generation by a strain of *Bacillus subtilis* in a microbial fuel cell. *J. Power Sources* **190**, 258–263 (2009).

46. Fan, Y. & Pedersen, O. Gut microbiota in human metabolic health and disease. *Nat. Rev. Microbiol.* **19**, 55–71 (2021).

47. Wu, F. et al. Modulation of microbial community dynamics by spatial partitioning. *Nat. Chem. Biol.* **18**, 394–402 (2022).

48. Zhou, H., Tai, J., Xu, H., Lu, X. & Meng, D. Xanthoceraside could ameliorate Alzheimer's Disease symptoms of rats by affecting the gut microbiota composition and modulating the endogenous metabolite levels. *Front. Pharmacol.* **10**, 1035 (2019).

49. Kong, C., Gao, R., Yan, X., Huang, L. & Qin, H. Probiotics improve gut microbiota dysbiosis in obese mice fed a high-fat or high-sucrose diet. *Nutrition* **60**, 175–184 (2019).

50. Gerritsen, J. et al. Characterization of *Romboutsia ilealis* gen. nov., sp. nov., isolated from the gastro-intestinal tract of a rat, and proposal for the reclassification of five closely related members of the genus *Clostridium* into the genera *Romboutsia* gen. nov., *Intestinibacter* gen. nov., *Terrisporobacter* gen. nov. and *Asaccharospora* gen. nov. *Int. J. System. Evol. Microbiol.* **64**, 1600–1616 (2014).

51. Zeng, Q. et al. Discrepant gut microbiota markers for the classification of obesity-related metabolic abnormalities. *Sci. Rep.* **9**, 13424 (2019).

52. Xu, H.-M. et al. Selection strategy of dextran sulfate sodium-induced acute or chronic colitis mouse models based on gut microbial profile. *BMC Microbiol.* **21**, 279 (2021).

53. Nadeau, P. et al. Prolonged energy harvesting for ingestible devices. *Nat. Biomed. Eng.* **1**, 0022 (2017).

54. Steiger, C. et al. Ingestible electronics for diagnostics and therapy. *Nat. Rev. Mater.* **4**, 83–98 (2019).

55. Mimee, M. et al. An ingestible bacterial-electronic system to monitor gastrointestinal health. *Science* **360**, 915–918 (2018).

56. Zhang, S. et al. A pH-responsive supramolecular polymer gel as an enteric elastomer for use in gastric devices. *Nat. Mater.* **14**, 1065–1071 (2015).

57. Lee, Y. et al. Therapeutic luminal coating of the intestine. *Nat. Mater.* **17**, 834–842 (2018).

58. Singh, J. S., Pandey, V. C. & Singh, D. P. Efficient soil microorganisms: a new dimension for sustainable agriculture and environmental development. *Agr. Ecosyst. Environ.* **140**, 339–353 (2011).

Methods

Chemicals

The liquid metal EGaIn was purchased from Indium Corporation with 75.5 wt% of gallium and 24.5 wt% of indium. The nanoclays, bentonite (cat. no. 682659) and halloysite (cat. no. 685445) were purchased from Sigma Aldrich. The tapioca starch (mean diameter of 10.09 ± 3.32 μm) was purchased from a local market.

Soil-inspired material fabrication

To prepare the soil-inspired material, we first added starch granules and nanoclay into deionized (DI) water in ratios from 1:1:8 to 1:1:18. The suspension was stirred overnight to ensure full hydration of the starch granules. We then added liquid metal into the well-dispersed suspension, followed by probe sonication for 5 min to break the liquid metal into nanoparticles and form a slurry. The liquid metal had the same weight as the nanoclay. We transferred the slurry into a design container for directional freezing in a cooling bath composed of dry ice and ethanol, with a cooling temperature of −72 °C. Once it was entirely frozen, we freeze-dried the sample overnight at 0.1-mbar pressure with a freeze dryer (Labconco, cat, no. 7670520) to form a layer-structured porous scaffold. Finally, we compressed the porous scaffold samples at 100 °C for 1 hour with a platen press (Dake, 44–225) to form the soil-inspired material with a pressure of 10 metric tonnes. We trimmed the soil-inspired material into desired shapes for the following experiments. The procedure was the same for the control sample without liquid metal, with the omission of the liquid metal during the probe sonication.

Ultramicrotomy sample preparation

The soil-inspired samples were infiltrated by a polymer resin (EpoThin 2 epoxy resin) in a vacuum chamber to fill the pores for imaging. The surfaces were polished on the polishing wheel with grit paper, and ion milling (Triple Beam ion miller, Leica TIC3X) was applied to polish the sample so that the soil-inspired material's cross-section was exposed to air. The samples were then ready for microtome or FIB experiments. In ultramicrotomy experiments, samples were mounted directly into a Leica UC7 ultramicrotome with a clamp-style chuck, and a block face was created with a diamond trimming tool. Sectioning occurred dry without a water trough using a 35° histo-cryo diamond knife (Diatome). In addition, 200-nm-thin sections were carefully collected with an eyelash manipulator made from a canine hair and deposited on a clamshell-style grid coated with formvar and 4 nm of carbon (EMS cat. no. GD1010-Cu).

X-ray fluorescence imaging and X-ray ptychography

X-ray fluorescence imaging and X-ray ptychography were performed using Bionanoprobe[59] at 9-ID-B in the Advanced Photon Source (APS) of Argonne National Laboratory. We prepared two different types of sample for X-ray fluorescent imaging and X-ray ptychography: (1) thin samples (~200 nm) produced using a microtome, as mentioned above, and secured on Si_3N_4 membranes and (2) a pyramid-shaped pillar (~20 μm in diameter). A coherent monochromatic X-ray beam (10.7-keV energy) was focused on the sample by a Fresnel zone plate into a spot of ~90 nm. While a sample was raster-scanned across the incident beam, full fluorescence spectra and diffraction patterns from each scan point were simultaneously recorded by a fluorescence detector and a pixelated area detector (Dectris Pilatus 300K), respectively, placed ~2.4 m downstream of the sample. For tomography data collection, the sample was rotated to a new angle with a 2° increment after finishing a 2D projection, until the whole 3D scan was completed. Thus, a total of 91 projections from an angular range of −90° to 90° were collected over ~18 hours, including experimental interruptions. Post-measurement data analysis included fluorescence spectrum fitting and quantification to construct elemental distributions, ptychography phase retrieval, image reconstruction and tomography reconstruction.

Fluorescence spectrum analysis was performed using MAPS, an IDL-based program developed in house[60]. The 2D ptychographic and fluorescence images were processed following the method in ref. [39]. In ptychographic reconstruction, the central 256 pixels × 256 pixels of each diffraction pattern were cropped, resulting in an image pixel size of 6.3 nm. Elemental fluorescence maps, including Ga, In and Si, were reconstructed from the collected fluorescence spectra using MAPS software. After excluding some low-quality projections, the best 85 projections of ptychographic and fluorescence images were used for tomography reconstruction. Images after reconstruction were also registered and analysed using VivoQuant 4.0 patch 1 (InviCRO). Ptychography measurements were collected using a custom code written in Python 2.8 with the PyEpics package.

SEM imaging

A scanning electron microscope (Carl Zeiss, Merlin) was used to image the morphology of multiple samples, including starch granules, the layer-structured porous scaffold and the soil-inspired material with/without laser writing. The SEM imaging was performed without sputter-coating conductive layers for the samples, including porous scaffold samples and soil-inspired samples with/without laser writing, to avoid disruption of the sample morphologies. The acceleration voltage of the scanning electron microscope was set at 2 kV. At least 20 measurements were performed for each sample to ensure consistency.

FIB

Cross-sectional images on soil-inspired material, the infiltrated and polished sample, were obtained with a FIB system (SPF FEI Helios FIB/SEM). The ion beam (30 kV, 0.46 nA) was used to sputter the substrate at a normal incidence angle, and the electron beam (5 kV, 1.4 nA) was used for imaging at 52°. A 10 μm × 10 μm region was etched with 4,000 passes to reveal the cross-sectional information. The images collected at 52° were stretched with the built-in angle correction function in Helios to produce images obtained at the cross-section's normal direction. Slices of the soil-inspired material were milled starting from the edge of the 10 μm × 10 μm region, with a slice thickness of 50 nm, to obtain the video. Electron-beam images were captured after milling each slice. The stacked images were made into videos using ImageJ with ten frames per second.

TEM imaging

TEM was performed on an FEI F30 system to image the nanoclay, liquid-metal particles and microtomed samples. The microtomed samples were imaged directly under the FEI F30 at 300 kV. Liquid-metal particles and nanoclay suspensions were diluted with DI water and dropped onto copper grids (Ted Pella, Lacey Formvar/Carbon, 200 meshes), and the samples were imaged under FEI F30 sytem at 300 kV after thorough drying.

STEM imaging

STEM was carried out using a 200-kV aberration-corrected JEOL ARM200F system with a cold field-emission source, which gives a spatial resolution of ~0.8 Å. The HAADF detector angle was set to 90–270 mrad to give Z contrast images. The low-angle annular dark-field (LAADF) detector angle was 40–120 mrad, and STEM EDS was carried out by an Oxford X-max 100TLE windowless SDD X-ray detector equipped with the JEOL ARM200F device.

ToF-SIMS

ToF-SIMS analysis was conducted on a Physical Electronics PHI TRIFT III secondary ion mass spectrometer. The primary beam was a gallium ion source with 15-kV energy. The positive ion spectra were collected in an area of 100 $μm^2$ for 3 min with/without laser-writing. Data were analysed using WinCadence software, and mass calibration was performed on hydrocarbon secondary ions.

Dynamic mechanical analyser test

The dynamic mechanical properties of the composites were measured with the three-point bending test. A machine (TA Instruments RSA-G2 dynamic mechanical analyser) with 10-μN resolution equipped with a three-point bending fixture was used to test specimens. Frequency sweeping was conducted over the range of 0.1–100 Hz under strain amplitudes of 0.01% to characterize the specimens' viscoelastic behaviour. The strain–stress curve was obtained under the three-point bending geometry at an angular frequency of 10 rad s^{-1}. All measurements were carried out in their linear viscoelastic region, determined by strain amplitude sweeping with a frequency of 1 Hz.

Nanoindentation

Nanoindentation was performed to characterize the soil-inspired material's mechanical properties with a Hysitron 950 TriboIndenter (Bruker) with a Berkovich indenter (three-sided pyramid-shaped diamond tip, tip radius of ~100 nm) in the ambient environment. The indentations were conducted at a constant loading and unloading speed of 20 μN s^{-1} to prevent potential time-dependent effects on the materials, such as viscoelastic behaviour on the nanoindentation test. The data were analysed using standard Oliver and Pharr analysis to extract the indentation moduli S (refs. [61,62]). The modulus of the soil-inspired material, E, can be further derived according to

$$E = \frac{1 - \upsilon_s^2}{\frac{1}{S} - \frac{1 - \upsilon_{diamond}^2}{E_{diamond}}},$$

where υ_s is the Poisson ratio of the samples (assuming υ_s is 0.3), $\upsilon_{diamond}$ is the Poisson ratio of the diamond tip ($\upsilon_{diamond} = 0.07$), and $E_{diamond}$ is the Young's modulus of the diamond ($E_{diamond} = 1{,}141$ GPa)[62].

Micro-computed tomography of soil-inspired material

Micro-computed tomography (microCT) images were captured on the XCUBE (Molecubes NV) at the Integrated Small Animal Imaging Research Resource (iSAIRR) at The University of Chicago. Spiral high-resolution CT acquisitions were performed with an X-ray source of 50 kV$_p$ and 440 μA. Volumetric CT images were reconstructed in a 1,400 × 1,400 × 750 format with voxel dimensions of 50 μm. Images were analysed using AMIRA 2020.1 (Thermo Fisher Scientific) and VivoQuant 4 patch 1 (InviCRO).

IR spectroscopy

For Fourier-transform infrared (FTIR) spectra, 15 mg starch powder and 5 μl of D$_2$O (Cambridge Isotope Laboratories) were held between two CaF$_2$ windows held in a temperature-regulated brass jacket. Temperature-dependent IR spectra were obtained using a Bruker Tensor 27 FTIR spectrometer by acquiring a series of spectra during a slow temperature ramp from 20 to 94 °C in 2 °C steps with a 60-s equilibration time between each spectrum. The sample temperature was monitored with a Phidget K-type thermocouple attached to the brass jacket. Attenuated total reflectance FTIR spectra were measured using a Bruker Platinum system.

DSC

DSC measurements were conducted using a TA Discovery DSC 2500 system with 5–10 mg of starch with different concentrations and conditions. The samples were measured at a heating and cooling rate of 10 °C min^{-1} from room temperature to 92 °C. The obtained data were processed by Trios software.

Laser sintering

Laser sintering was performed on soil-inspired material and control samples with a CO$_2$ laser cutter (Universal Laser Systems, VLS 4.60) with raster and vector modes. In both operation modes, the sintering power was 2%, 5% and 10% (referred to as low, medium and high power, respectively), the speed was 20%, and the patterning procedure was repeated twice to obtain the desired engraving. We laser-wrote a library of patterns using a combination of vector and raster modes with the 5% sintering power setting.

Optical microscope imaging

Bright-field images were taken with a Nikon Eclipse Ti2 microscope to analyse the starch granule morphology in the hydrated state. Starch granules were suspended in DI water and hydrated overnight, and the solution was directly transferred onto the microscope glass slides for measurements. The average size of the starch granules was calculated with ~700 particles.

Laser confocal scanning microscope imaging

A 3D laser confocal scanning microscope (LEXT OLS5000) was utilized to characterize the soil-inspired material's surface morphology with laser writing. The obtained images contained surface roughness and height information for the patterns. The images were coloured based on height information on the surface to visualize the conductive patterns.

XANES

XANES measurements were performed at the Advanced Photon Source APS/CNM beamline 26-ID-C at Argonne National Laboratory. XANES data were collected by scanning X-ray excitation energies across the absorption edge of the element of interest and measuring the intensity of Kα fluorescence at each energy. A Si(111) double-crystal monochromator was used to select the X-ray energy. The monochromator energy was calibrated with standard Zn metal foil before XANES measurements. To measure XANES of the Ga element, excitation energies were scanned from 10,335 eV to 10,410 eV in 0.5-eV increments. A fluorescence spectrum was collected for 1 s for each excitation energy, and Ga Kα-emission intensity was represented by integrating the signal over a properly defined region of interest in the spectrum. Each scan was performed twice, and the results were averaged. The fluorescence intensity was then normalized to the incident X-ray intensity to calculate the absorption coefficient for each excitation energy. Liquid gallium and gallium oxide were used to compare the samples' absorption edge energy to compounds of known oxidation states. To compare samples and standards under a similar signal lever, the calculated coefficient profiles were further normalized over their respective post-edge coefficient averaged from 10,391 eV to 10,401 eV.

Conductivity and solvent test

To measure the real-time changes in resistance, we built a voltage-divider circuit using a Data Acquisition (DAQ, National Instruments, USB-6210) device and a LabVIEW program (Supplementary Fig. 51). Soil-inspired materials with mechanically sintered conductive paths were exposed to different solvents, including acetone, benzene, dichloromethane, diethyl ether, dimethylformamide, dimethyl sulfoxide, ethanol, glycerol, hexane, IPA, methanol, methyl acetate, THF, toluene and *o*-xylene, with multiple replicate samples ($N > 6$). The resistance of the soil-inspired material was recorded over time.

Biofilm growth on soil-inspired materials

Bacillus subtilis biofilms were grown in an MSgg minimal medium agar plate containing 5 mM potassium phosphate buffer, 100 mM MOPS buffer (pH 7.0 adjusted with NaOH), 2 mM MgCl$_2$, 700 μM CaCl$_2$, 50 μM MnCl$_2$, 100 μM FeCl$_3$, 1 μM ZnCl$_2$, 2 μM thiamine hydrochloride, 0.5% (vol/vol) glycerol, 0.5% (wt/vol) monosodium glutamate, 50 μg ml^{-1} tryptophan and 50 μg ml^{-1} phenylalanine. Typically, the soil-inspired material was centred on the Msgg agar plate, and 3 μl of *B. subtilis* culture was transferred onto the centre of the material. After culturing at 30 °C for two days, the biofilm growth area was measured by ImageJ.

Bacillus subtilis and *E. coli* growth in liquid flask culture

Bacillus subtilis bacteria were cultured in 4 ml of LB medium at 37 °C overnight. We transferred 1% overnight culture to 30 ml of MSgg liquid culture supplemented with soil-inspired material, carbon paper, polyacrylamide hydrogel or organic potting soil and grew the culture in a rotary shaker at 37 °C for 12 hours. The colony-forming units per millilitre method was used to measure the biomass of cultured *B. subtilis*.

Escherichia coli bacteria were cultured in 4 ml of LB medium at 37 °C overnight. We transferred 1% overnight culture to 30 ml of M9 minimum medium (containing 4 g l^{-1} glucose) supplemented with soil-inspired material and grew the culture in a rotary shaker at 37 °C for 12 hours. The biomass of the *E. coli* was measured using the colony-forming unit method. Fermentation products were measured by HPLC (1200 series, Agilent Technologies) with a mobile phase of 4 mM H$_2$SO$_4$ using an Aminex HPX-87H column with a Micro Guard Cation H Cartridge. The column temperature was set to 55 °C, and the flow rate was 0.6 ml min^{-1}.

Biocompatibility test

C57BL/6J mice (6–8 weeks) were orally administered a daily dose of 75 mg kg^{-1} soil-inspired material powder for seven consecutive days. Body weights (days 0–7) were recorded every day before oral gavage. On day 7, all the mice were euthanized. Colons were collected for length measurement and histology in the Human Tissue Resource Center at the University of Chicago. Crypt nuclei number and crypt depth were quantified on the colon histology scans. Other internal organs, including the liver, heart and kidney, were also collected for histological examination. The glomerulus area was quantified on the kidney histology scans. All animals were housed under pathogen-free conditions, and all animal procedures were approved by the Institutional Animal Care and Use Committee (IACUC) of the University of Chicago.

Ribosomal 16S sequencing

C57BL/6J mice (6–8 weeks) were orally administered a daily dose of 75 mg kg^{-1} soil-inspired material powder for seven consecutive days. Two groups of faeces samples (control and soil-inspired material) were collected for 16S sequencing. A test on the tetracycline-induced dysbiosis model was also conducted. Briefly, mice were orally administered with two doses of 10 mg kg^{-1} tetracycline (suspended in 2.5% sodium carboxymethylcellulose) for two days. Mice in the control group were given the same dose of vehicle. Two groups of faeces samples (CMC.Day2, Tet.Day2) were collected for 16S sequencing. After day 3, tetracyclin-treated mice were orally administered with 75 mg kg^{-1} soil-inspired material (suspended in water) for seven days. Two groups of faeces samples (Tet.Day2.ctrl.Day7, Tet.Day2.LM.Day7) were collected for 16S sequencing.

Faeces samples were processed and analysed with the ZymoBIOMICS Targeted 16S Sequencing Service (Zymo Research). Unique amplicon sequence variants were inferred from raw reads using the DADA2 pipeline[63]. Potential sequencing errors and chimaeric sequences were removed with the DADA2 pipeline. Chimaeric sequences were also removed with the DADA2 pipeline. Taxonomy assignment was performed using Uclust from Qiime v.1.9.1 with the Zymo Research Database, a 16S database that is internally designed and curated as a reference. Composition visualization, alpha-diversity and beta-diversity analyses were performed with Qiime v.1.9.1[64]. Taxonomy with significant abundance among different groups was identified by LEfSe using default settings[40,65–71]. Other analyses, such as heatmaps, Taxa2ASV Decomposer and principal coordinate analysis plots, were performed with internal scripts. Absolute abundance was quantified with quantitative real-time polymerase chain reaction. The resulting values were shown as the gene copies number.

DSS model of ulcerative colitis

For DSS-induced colitis animal tests, C57B/6J mice (6–8-weeks old) were given 2% DSS drinking water ad libitum for seven days. Soil-inspired material, composed of starch, nanoclay and liquid metal, as well as different two-component combinations, were administered through oral gavage into the mouse stomach at a dose of 75 mg per kg body weight once a day in concurrence with DSS treatment. All animals were euthanized at the endpoint. Colitis symptoms were evaluated based on daily body weight, faecal blood test, postmortem colon length, faecal water content and colonic histology exams. Faecal blood scores were calculated with the following scoring system: 0, normal stool consistency with negative haemoccult; 1, soft stools with positive haemoccult; 2, very soft stools with traces of blood; 3, watery stools with visible rectal bleeding. Histological injury scores were calculated based on the following aspects of haematoxylin-and-eosin-stained colonic tissue sections: severity of inflammation (0–3: none, slight, moderate, severe), the extent of injury (0–3: none, mucosal, and submucosal, transmural) and crypt damage (0–4: none, basal one-third damaged, basal two-thirds damaged, only surface epithelium intact, entire crypt and epithelium lost). Faecal samples were collected for colonic microbiome analysis with 16S rRNA sequencing.

MicroCT of soil-inspired material in gastrointestinal region

Mice were prepared following an overnight fast and receiving oral gavage with soil-inspired material for in vivo monitoring. Mice were imaged by microCT (XCUBE, Molecubes NV) by the Integrated Small Animal Imaging Research Resource (iSAIRR) at The University of Chicago. The first scan was performed before any gavage procedure and scanned immediately after oral administration as time 0, then scanned at 1, 2, 3, 4 and 6 hours, respectively. Once those scans were completed, mice were euthanized, and gastrointestinal tissue was collected for ex vivo microCT scan. Spiral high-resolution CT acquisitions were performed with an X-ray source of 50 kV$_p$ and 440 µA. Volumetric CT images were reconstructed in a 400 × 400 × 1,200 format with voxel dimensions of 100 µm^3. Images were analysed using AMIRA 6.4 (Thermo Fisher Scientific) and VivoQuant 3.5 patch 2 (InviCRO).

Statistics and reproducibility

Data were statistically analysed with ordinary one-way ANOVA and Tukey's multiple comparisons test unless specified in the figure legends. For materials characterizations, all the SEM or TEM images were individually repeated more than five times at different sample spots. The X-ray ptychography and fluorescence imaging were repeated twice. Bacterial experiments were individually repeated at least three times. Animal experiments were individually repeated three times, except for the DSS-induced colitis test.

Reporting summary

Further information on research design is available in the Nature Research Reporting Summary linked to this Article.

Data availability

All data supporting the findings of this study are available within the Article, its Supplementary Information and Supplementary Files. Data are also available from the corresponding authors upon reasonable request. Source data are available at https://osf.io/muc9g/?view_only=971b8fde8562427ab619bc30c2624cb7. Source data are provided with this Paper.

Code availability

For PtychoShelves, code is available at https://www.psi.ch/en/sls/csaxs/software, and for PtychoLib, at https://github.com/kyuepublic/ptychopy.

References

59. Chen, S. et al. The Bionanoprobe: hard X-ray fluorescence nanoprobe with cryogenic capabilities. *J. Synchrotron Radiat.* **21**, 66–75 (2014).

60. Vogt, S. MAPS: a set of software tools for analysis and visualization of 3D X-ray fluorescence data sets. *J. Phys. IV Proc.* **104**, 635–638 (2003).

61. Oliver, W. C. & Pharr, G. M. An improved technique for determining hardness and elastic modulus using load and displacement sensing indentation experiments. *J. Mater. Res.* **7**, 1564–1583 (1992).

62. Oliver, W. C. & Pharr, G. M. Measurement of hardness and elastic modulus by instrumented indentation: advances in understanding and refinements to methodology. *J. Mater. Res.* **19**, 3 (2004).

63. Callahan, B. J. et al. DADA2: high-resolution sample inference from Illumina amplicon data. *Nat. Methods* **13**, 581–583 (2016).

64. Caporaso, J. G. et al. QIIME allows analysis of high-throughput community sequencing data. *Nat. Methods* **7**, 335–336 (2010).

65. Segata, N. et al. Metagenomic biomarker discovery and explanation. *Genome Biol.* **12**, R60 (2011).

66. Max, J.-J. & Chapados, C. Isotope effects in liquid water by infrared spectroscopy. III. H_2O and D_2O spectra from 6,000 to 0 cm^{-1}. *J. Chem. Phys.* **131**, 184505 (2009).

67. Bodis, P., Larsen, O. F. A. & Woutersen, S. Vibrational relaxation of the bending mode of HDO in liquid D_2O. *J. Phys. Chem. A* **109**, 5303–5306 (2005).

68. Sekkal, M., Dincq, V., Legrand, P. & Huvenne, J. P. Investigation of the glycosidic linkages in several oligosaccharides using FT-IR and FT Raman spectroscopies. *J. Mol. Struct.* **349**, 349–352 (1995).

69. Cael, S. J., Koenig, J. L. & Blackwell, J. Infrared and Raman spectroscopy of carbohydrates: Part III: Raman spectra of the polymorphic forms of amylose. *Carbohydr. Res.* **29**, 123–134 (1973).

70. Liu, Q., Charlet, G., Yelle, S. & Arul, J. Phase transition in potato starch-water system I. Starch gelatinization at high moisture level. *Food Res. Int.* **35**, 397–407 (2002).

71. Cael, J. J., Koenig, J. L. & Blackwell, J. Infrared and Raman spectroscopy of carbohydrates. Part VI: normal coordinate analysis of V-amylose. *Biopolymers* **14**, 1885–1903 (1975).

Acknowledgements

Author contributions

B.T. supervised the research. Y.L. and B.T. conceived the idea. Y.L., X.G., J.Y. and B.T. developed the methods. Y.L., X.G., J.Y., Y.F., J.S., L.M., C.C., X.-X.Z., H.-M.T., F.S., J.H., Q.T., E.W.R., R.B., X.C., P.G., Z.C., J.D., S.C. and A.P. performed the experiments. Y.J., J.Y., H.-M.T. and F.M. analysed and processed the data. Y.L., X.G., J.Y. and B.T. wrote the paper, with comments from all authors.

Competing interests

The authors declare no competing interests.

Additional information

Supplementary information The online version contains supplementary material available at https://doi.org/10.1038/s41557-022-01064-2.

Correspondence and requests for materials should be addressed to Yiliang Lin or Bozhi Tian.

Peer review information *Nature Chemistry* thanks the anonymous reviewer(s) for their contribution to the peer review of this work.

Reprints and permissions information is available at www.nature.com/reprints.

nature research

Corresponding author(s): Bozhi Tian, Yiliang Lin

Last updated by author(s): Aug 5, 2022

Reporting Summary

Nature Research wishes to improve the reproducibility of the work that we publish. This form provides structure for consistency and transparency in reporting. For further information on Nature Research policies, see our Editorial Policies and the Editorial Policy Checklist.

Statistics

For all statistical analyses, confirm that the following items are present in the figure legend, table legend, main text, or Methods section.

n/a	Confirmed	
☐	☒	The exact sample size (*n*) for each experimental group/condition, given as a discrete number and unit of measurement
☐	☒	A statement on whether measurements were taken from distinct samples or whether the same sample was measured repeatedly
☐	☒	The statistical test(s) used AND whether they are one- or two-sided *Only common tests should be described solely by name; describe more complex techniques in the Methods section.*
☐	☒	A description of all covariates tested
☐	☒	A description of any assumptions or corrections, such as tests of normality and adjustment for multiple comparisons
☐	☒	A full description of the statistical parameters including central tendency (e.g. means) or other basic estimates (e.g. regression coefficient) AND variation (e.g. standard deviation) or associated estimates of uncertainty (e.g. confidence intervals)
☐	☒	For null hypothesis testing, the test statistic (e.g. F, t, r) with confidence intervals, effect sizes, degrees of freedom and P value noted *Give P values as exact values whenever suitable.*
☒	☐	For Bayesian analysis, information on the choice of priors and Markov chain Monte Carlo settings
☒	☐	For hierarchical and complex designs, identification of the appropriate level for tests and full reporting of outcomes
☒	☐	Estimates of effect sizes (e.g. Cohen's *d*, Pearson's *r*), indicating how they were calculated

Our web collection on statistics for biologists contains articles on many of the points above.

Software and code

Policy information about availability of computer code

Data collection The fluorescence imaging data were collected with MAPS, an IDL-based program developed in-house (J. Phys. IV Proc. 2003, 104, 635–638). Ptychography measurements were collected using a custom code written in Python 2.8 with PyEpics package(3.3.3).

Data analysis Scanning electron microscopy data were analyzed using ImageJ 1.52a. Transmission electron microscopy or scanning transmission electron microscopy data were analyzed using DigitalMicrograph 3.42.3048.0, ImageJ 1.52a and AZtec4.3.2D ptychographic reconstructions were processed using a GPU open source library, Ptycholib, written in C++. 3D ptychography was reconstructed by PtychoShelves in Matlab R2018a. The ptychography and fluorescence images after reconstruction were also registered and analyzed using VivoQuant 4.0 patch 1. Plottings were performed with Origin 2019b (32-bit) 9.6.5.169 and Adobe Illustrator 21.0.0. Laser confocal scanning microscope images were analyzed with OLYMPUS OLS 5000 1.1.1.55. Micro-CT data were analyzed using Amira 5.6.Histology images and data were analyzed with CaseViewer 2.4. Optical images were analyzed with ImageJ 1.52a. TOF-SIMS data were analyzed with WinCadence software. Statistical analysis were performed with Graphpad Prism 9.4.0.

For manuscripts utilizing custom algorithms or software that are central to the research but not yet described in published literature, software must be made available to editors and reviewers. We strongly encourage code deposition in a community repository (e.g. GitHub). See the Nature Research guidelines for submitting code & software for further information.

Data

Policy information about availability of data

All manuscripts must include a data availability statement. This statement should provide the following information, where applicable:

- Accession codes, unique identifiers, or web links for publicly available datasets
- A list of figures that have associated raw data
- A description of any restrictions on data availability

All the data supporting the findings of this study are available within the paper, the supplementary materials or the source data. The data are available from the corresponding authors upon reasonable request. Source data are also available at https://osf.io/muc9g/?view_only=971b8fde8562427ab619bc30c2624cb7

Field-specific reporting

Please select the one below that is the best fit for your research. If you are not sure, read the appropriate sections before making your selection.

☒ Life sciences ☐ Behavioural & social sciences ☐ Ecological, evolutionary & environmental sciences

For a reference copy of the document with all sections, see nature.com/documents/nr-reporting-summary-flat.pdf

Life sciences study design

All studies must disclose on these points even when the disclosure is negative.

Sample size	Sample size was determined based on extensive laboratory experience and literature in the field. The number of biological replicates we aimed for was at least 3 with technical replicates in each group so that the number of biological and technical replicates is necessary to convince us that the effect was real. The number of biological replicates in animal test was at least 5 in each group.
Data exclusions	Representative images were shown in the manuscripts; similar results from experimental repeats were not shown. No data excluded for statistical analyses.
Replication	All experimental findings, including TEM and SEM images, Micro-CT images, confocal laser microscopy images, EDS spectra, FTIR spectra, TOF-SIMS spectra, x-ray fluorescence and ptychography, bacteria experiments and animal experiments, were reliably reproduced. For materials characterizations, all the SEM or TEM images were individually repeated more than five times at different sample spots. The X-ray ptychography and fluorescence imaging were repeated two times. Bacterial expriments were individually repeated for at least three times. Animal experiments were individually repeated three times except the DSS-induced colitis test in figure 5 was only done once. These experiments were replicated from every week to every month and all the experiments were successful.
Randomization	Experimental groups were formed based on what was being tested with random sections. The same type of material, bacterial cells and animals were used for all experiments. The bacteria from the same flask culture were randomly allocated into different groups for testing the modulation activity of the materials. The animals were purchased from the Jackson Laboratory and were randomly allocated into different groups for testing the modulation activity of the materials. The same ratio/number of commercially purchased male and female mice were randomly allocated into all individual experimental groups. These mice were all in the same age range (6-8 weeks) and body weight range (20-25 grams).
Blinding	Experimenters were blinded during imaging experiments. Biocompatibility tests and tetracyclin-treated experiments were not performed blind to the conditions of the experiments as treatments were determined beforehand and animal were selected in order to acquire sufficient sample size per experimental group. All subsequent samples were blinded to group allocation during data collection and analysis.

Reporting for specific materials, systems and methods

We require information from authors about some types of materials, experimental systems and methods used in many studies. Here, indicate whether each material, system or method listed is relevant to your study. If you are not sure if a list item applies to your research, read the appropriate section before selecting a response.

Materials & experimental systems

n/a	Involved in the study
☒	☐ Antibodies
☒	☐ Eukaryotic cell lines
☒	☐ Palaeontology and archaeology
☐	☒ Animals and other organisms
☒	☐ Human research participants
☒	☐ Clinical data
☒	☐ Dual use research of concern

Methods

n/a	Involved in the study
☒	☐ ChIP-seq
☒	☐ Flow cytometry
☒	☐ MRI-based neuroimaging

Animals and other organisms

Policy information about studies involving animals; ARRIVE guidelines recommended for reporting animal research

Laboratory animals

6-8 week old C57BL/6J mice (female and male) purchased from the Jackson Laboratory were used in in vivo biocompatibility experiments (tissue harvesting after euthanasia for H&E staining, fecal sample collecting and body weight monitoring).
Mice were housed in the animal facility of the University of Chicago. The animal room was maintained in an environment with the humidity of 40-60 % and the temperature of 18-23 °C under a 12-h light/12-h dark cycle. The animals were allowed free access to food and water.All animal procedures were approved by the Institutional Animal Care and Use Committees (IACUC) of the University of Chicago under the protocol # 72621."

Wild animals

No wild animals were used.

Field-collected samples

No field-collected samples were used.

Ethics oversight

All animals were housed under pathogen-free conditions and all animal procedures were approved by the Institutional Animal Care and Use Committees (IACUC) of the University of Chicago.

Note that full information on the approval of the study protocol must also be provided in the manuscript.